MECHANICAL ALLOYING SYNTHESIS OF FORSTERITE-DIOPSIDE NANOCOMPOSITE POWDER FOR USING IN TISSUE ENGINEERING

SOROUR SADEGHZADE, RAHMATOLLAH EMADI, #HAMED GHOMI

Department of Materials Engineering, Isfahan University of Technology, Isfahan 84156-83111, Iran

#E-mail: hamed1985.gh@gmail.com, hamed.ghomi@ma.iut.ac.ir

In present study the pure forsterite-diopside nanocomposite powder was successfully synthesized by the economical method of mechanical alloying and subsequence sintering, for the first time. The starting economical materials were talc ($Mg_3Si_4H_2O_{12}$), magnesium carbonate ($MgCO_3$) and calcium carbonate ($CaCO_3$) powders. The prepared powder was characterized by thermo gravimetric analysis (TGA), X-ray diffraction (XRD), and scanning electron microscopy (SEM). The results showed preparation of forsterite- diopside nanocomposite powder after 10 h mechanical alloying and sintering at 1200°C for 1 h. The powder crystallite sizes and agglomerated particle sizes were measured about 73 ± 4 nm and 0.3 - 4 µm, respectively. Absence of enstatite that causes a reduction in mechanical and bioactivity properties of forsterite ceramic, is an important feature of produced powder.

INTRODUCTION

An improved understanding of currently used bioceramics in human implants and bone replacement materials could contribute significantly to the design of new-generation prostheses and post-operative patient management strategies [1]. In recent years many of researchers have shown that bioceramics based on Si, Ca and Mg have good properties such as: bioactivity, biocompatibility, high compressive strength and wear resistance with human body constituents in comparison to hydroxyapatite (HA); furthermore release of Mg, Si and Ca ions from these materials in many cases showed to have good effect on cell proliferation, differentiation and adhesion [2].

Forsterite (Mg_2SiO_4) is a member of the olivine family of crystals in the $MgO–SiO_2$ system. Previous studies have shown that forsterite has better mechanical properties compared to HA [3-5]. Kharaziha and Fathi have shown that nanoforsterite ceramic powder has fracture toughness and micro hardness of about 3.61 ± 0.1 MPa m$^{1/2}$ and 940 ± 10 HV, respectively which are high in comparison to HA with 0.75 - 1.2 MPa·m$^{1/2}$ fracture toughness and 700 HV microhardness [6]. Microforsterite powder is cytocompatible and exhibits good mechanical properties, very low degradation

and no HA precipitation on its surface; while it has been shown that nanoforsterite has good bioactivity, biocompatibility, apatite-formation ability in human body and degradation rate increase in biological fluids; therefore forsterite has been suggested as a bioceramic for bone repair applications and hard tissue engineering [5, 7-10].

Diopside ($CaMgSi_2O_6$) is the member of pyroxene minerals. Dens diopside (3.2 g·cm^{-3}) in comparison to HA (3.16 g·cm^{-3}) has fairly high mechanical properties such as 3.5 MPa·m$^{1/2}$ fracture toughness and 170 GPa young's modulus [11]. Previous studies have shown that diopside has good apatite-formation ability on its surface and this layer which formed on diopside is similar to natural cortical bone and also dentine. Diopside is capable of inducing osteogenesis in biological fluids and a good bioactive material for hard tissue engineering while it is not cytotoxic [12-14].

Nanostructure and nanocrystalline ceramics in comparison to microparticle ceramics have improved properties such as high contact area, high diffusion rates, reduced sintering time or temperature, and high mechanical properties. For example nanocrystalline HA improves osteoblast cells adhesion, differentiation, proliferation, osteointegration and Ca containing minerals deposition on its surface better than microcrystalline

HA [15-16].

Mechanical alloying (MA) is the most effective way of nanomaterials fabrication. MA method offers a simple, novel, powerful and economical method of nanomaterials fabrication in comparison to sol-gel method which is a time consumer and expensive method despite its lower contamination compared to MA [17-19].

Considering the nature of bones and teeth as natural nanocomposites, the use of bioceramics as nanocomposites can produce optimized properties [16].

Considering the properties of diopside and forsterite, the combination of these bioceramics has been useful for obtaining nanocomposite materials with high mechanical and bioactivity properties.

Present study was aimed to produce forsterite-diopside nanocomposite powder via MA method in order to use their high mechanical and biological properties. This nanocomposite powder can be used in tissue engineering applications.

EXPERIMENTAL

Powder preparation

Forsterite-diopside nanocomposite powder was prepared by talc ($Mg_3Si_4H_2O_{12}$) (98 % purity, Merck), magnesium carbonate ($MgCO_3$) (98 % purity, Aldrich) and calcium carbonate ($CaCO_3$) (98 % purity, Merck) powders. In order to produce the powder, talc, $MgCO_3$ and $CaCO_3$ powders with molar ratio of 1:2:1 were mixed in a high energy ball mill with steel vial and balls with 2 cm diameter. The ball/powder mass ratio was 10:1 and the rotational speed of disc was set 445 rpm. The time of MA was chosen 10 minutes, 2, 5 and 10 h and these samples were sintered at 1200°C for 1 h.

Characterization of nanocomposite powder

Thermo gravimetric analysis (TGA) was used for finding calcination temperature of talc, $MgCO_3$ and $CaCO_3$ and crystallization temperature of forsterite and diopside powders. For this purpose, initial mixed powders after 10 minutes and 10 h MA were used. The powders were characterized via TGA from room temperature up to 1200°C under flowing nitrogen gas at a heating rate of 20°C·min^{-1}.

Crystallite size and phase transformation assessment during MA were assigned by X-ray diffraction (XRD) with Cu K$_\alpha$ radiation ($\lambda = 0.154$ nm at 20 kV and 30 mA). The XRD patterns were recorded in the 2θ range of 20°-80° (step size 0.05° and time per step 1 s). The crystallite sizes were measured by Williamson- Hall method [20].

$$\beta \cos \theta = \frac{0.9\lambda}{D} + 2\varepsilon \sin \theta \qquad (1)$$

where θ is the Bragg diffraction angle, ε internal strain,

D the crystallite size, λ the wavelength of the radiation, β the diffraction peak width at half maximum intensity, and 0.9 the Scherrer constant. The particles' morphology of powder was shown by scanning electron microscopy (SEM) in a Philips XL30 at an acceleration voltage of 30 kV. SEM images were used for measuring the particle sizes of forsterite- diopside nanocomposite powder.

RESULT AND DISCUSSION

Thermo gravimetric analysis

TGA curves corresponded to10 minutes (A) and 10 h (B) MA have been presented in Figure 1. The first weight loss of 10 minutes mixed powders was occurred below 300°C due to the loss of hydration water of the mixed powders. The thermal decomposition of $MgCO_3$ and $CaCO_3$ and crystallization of CaO and MgO was occurred between 300 to 420°C and 500 to 700°C, respectively. The fourth stage was corresponded to decomposition and release of structural water of talc and crystallization of forstrite and diopside. This stage was occurred between 800°C to 1200°C.
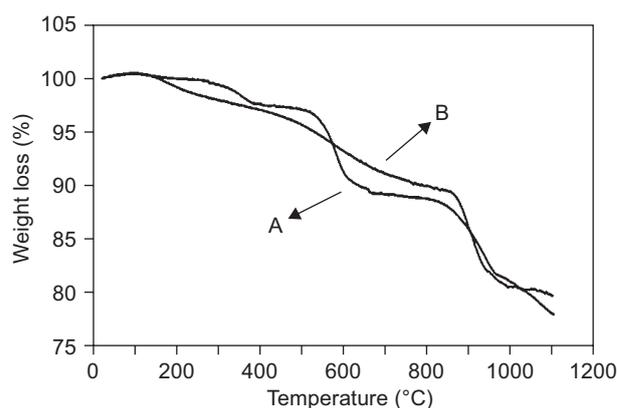
Figure 1. TG curves corresponded to (A) 10 minutes and (B) 10 h MA of the mixed powders.

The obtained results were in agreement with the results of other researchers [21-22]. Tavangarian and Emadi reported the range of 300 - 500°C for decomposition of $MgCO_3$ and talc, and 900 - 1200°C for crystallization of MgO and forsterite. Petask et al. reported the exact temperature of 692°C for decomposition of $CaCO_3$ and crystallization of CaO. They also reported 800 - 1150°C temperature range for decomposition of talc and crystallization of diopside.

Figure 1B also shows an improvement in the kinetic of reactions by increasing MA time from 10 minutes to 10 h. by increasing the MA time, the rate of reactions was increased and the reactions were occurred in lower temperatures which was due to the reduction of particles size with MA. Particle size reduction, increases the specific surface area and internal energy and causes diffusion rate increment and accelerates the reactions.

X-ray diffraction analysis

Figure 2 shows the XRD patterns of specimens after different MA time without any heat treatment. Figure 2a shows XRD pattern of the starting materials and those had good agreement with the standards for $MgCO_3$ [23], $CaCO_3$ [24] and talc [25] compiled by the Joint Committee on Powder Diffraction and Standards (JCPDS).

Figure 2b shows the XRD pattern of powder after 2 h MA. As seen in Figure 2 the characteristic peaks correspond to $MgCO_3$, $CaCO_3$, talc, CaO [26], and SiO_2 [27]. The intensity of talc, $MgCO_3$ and $CaCO_3$ peaks were decreased in Figure 2b in comparison to Figure 2a. Also some peaks of talc, $MgCO_3$ and $CaCO_3$ were disappeared and the SiO_2 and CaO peaks were appeared due to decomposition of talc, $MgCO_3$ and $CaCO_3$. Increasing MA time by decomposition of materials and decreasing the particle size, caused a reduction in peaks intensity and an increase in peaks width.

Figure 2d presents the XRD pattern of 10 h MA. As shown in Figure 2d the characteristic peaks correspond to SiO_2 and CaO. The MgO [28] peaks were appeared at 5 h MA and disappeared at 10 h MA. Figure 2d compared to Figure 2a, b, and c, shows disappearing of $CaCO_3$, $MgCO_3$, and talc peaks and an increase in the intensity of SiO_2 and CaO peaks.

peaks of MgO, CaO, enstatite, forsterite [31], and diopside [32] were observed. Figure 3b presents the XRD pattern of sintered powder with 5 h MA. As seen in Figure 3 the characteristic peaks correspond to MgO, CaO, enstatite, forsterite and diopside. In Figure 3b in comparison to Figure 3a, the peaks correspond to MgO, and some of CaO and enstatite peaks were disappeared and the intensity of CaO and enstatite peaks were decreased which was due to the reaction of enstatites with CaO, MgO and SiO_2 and the formation of forsterite and diopside bioceramics. Figure 3c shows the XRD pattern of sintered powder with 10 h MA. The XRD pattern only shows the characteristic peaks of forsterite and diopside. Therefore, after 10 h MA the formation of forsterite-diopside nanocomposite powder was completed. The crystallite sizes of prepared powders could be measured by broadening of peaks of diffraction patterns. The crystallite sizes of forsterite-diopside nanocomposite powders were determined by WilliamSon-Hall equation [20]. The crystallite sizes of the sintered powders after 2 h, 5 h and 10 h MA were measured about 87 ± 2, 81 ± 2, and 73 ± 4 nm, respectively.
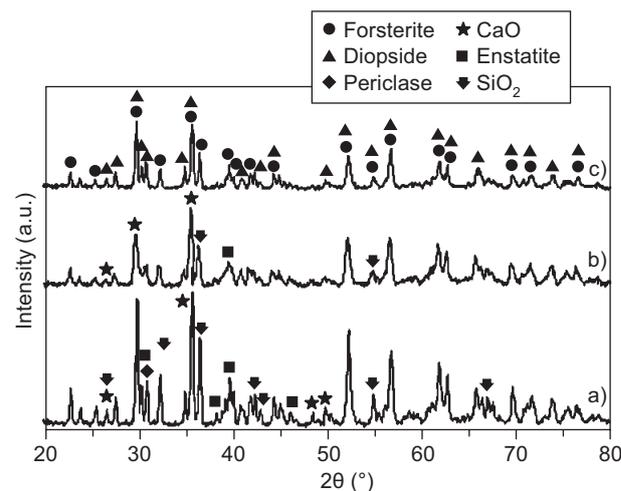
Figure 3. X-ray diffraction patterns of the prepared powder after mechanical alloying for various times and subsequent sintering at 1200°C for: a) 2 h, b) 5 h, and c) 10 h.

Figure 2. X-ray diffraction patterns of starting materials after mechanical alloying for various times: a) 10 minutes, b) 2 h, c) 5 h, and d) 10 h.

The sintering temperature for forsterite and diopside powder in related studies has been reported between 1000 - 1400°C [4, 11, 29]. In this study as shown Figure 1, the sintering temperature for forsterite-diopside nanocomposite fabrication was chosen 1200°C for 1 h. Figure 3 shows the XRD patterns of powder after various MA time with heat treatment at 1200°C for 1 h. Figure 3a shows the XRD pattern of sintered powder with 2 h MA. As seen in Figure 3a), the decomposition of talc to SiO_2 and enstatite [30] was occurred also the characteristic

Mechanism and kinetic of forstrite and diopside formation

As for Figures 1, 2 and 3, thermodynamics information and Gibs free energy of reactions, decomposition reactions of $MgCO_3$, $CaCO_3$ and talc were happened according to below Equations, respectively:

$$MgCO_3 \rightarrow MgO + CO_2$$
$$\Delta G_{1200\,°C} = -132.81 \text{ KJ mol}^{-1} \text{ K}^{-1} \tag{2}$$

$$CaCO_3 \rightarrow CaO + CO_2$$
$$\Delta G_{1200\,°C} = -43.712 \text{ KJ mol}^{-1} \text{ K}^{-1} \tag{3}$$

$$Mg_3Si_4O_{12}H_2 \rightarrow 3MgSiO_3 + SiO_2 + H_2O$$
$$\Delta G_{1200\,°C} = -33.59 \text{ KJ mol}^{-1} \text{ K}^{-1} \tag{4}$$
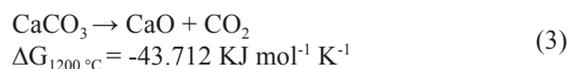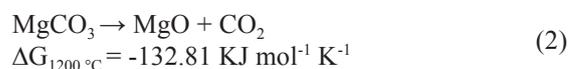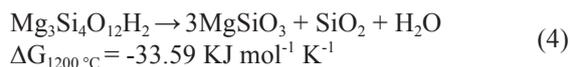
As for TGA and XRD results, top reactions were occurred in prepared powder with various MA time by sintering at 1200°C less than 1 h. This is in agreement with Tavangarian and Emadi results about decomposition of $MgCO_3$, $CaCO_3$ and talc [21]. Enstatite is a member of MgO–SiO_2 system. Enstatite has good properties (for example K_{IC} = 2.4 MPa·m$^{1/2}$) in compartion to HA (K_{IC} = 0.75 - 1.2 MPa·m$^{1/2}$); but its mechanical and bioactivity properties are less than forsterite and diopside [5, 11, 33]. The presence of enstatite causes a decrease in mechanical and bioactivity properties of this nanocomposite powder. Enstatite has four different polymorphs and they are unstable [33-34] and it is a special feature. In this study, enstatite phase was disappeared because of the reaction with MgO and formation of forsterite and also the reaction with CaO and SiO_2 and formation of diopside. Enstatite could be produced considering equation (4) and the following equation:

$$SiO_2 + MgO \rightarrow MgSiO_3$$
$$\Delta G_{1200\,°C} = -14.49 \text{ KJ mol}^{-1} \text{ K}^{-1} \tag{5}$$
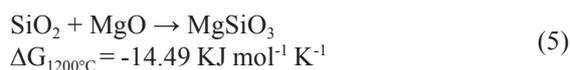
Enstatite from these two reactions changes to forsterite and diopside according to Equation 6 and Equation 7:

$$MgSiO_3 + MgO \rightarrow Mg_2SiO_4$$
$$\Delta G_{1200\,°C} = -30.25 \text{ KJ·mol}^{-1}·\text{K}^{-1} \tag{6}$$
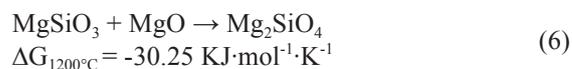
Adiabatic temperature is an appropriate criterion to determine the mechanism of reaction. The minimum temperature required for processing of self- propagating combustion is 1527°C [35]. If the adiabatic temperature of reaction was less than 1527°C, the reaction would occur in diffusion form.

According to the calculated adiabatic temperature for forsterite formation (T_{ad} = 220°C), Equation 6 was processed in diffusion mode. These results were in agreement with the results of Brindlly and Hayami [36]. These researchers have shown that MgO initially reacted at the surface of the SiO_2 to form enstatite, then the diffusion of MgO through the enstatite layer occured.

As seen in Figure 1 diopside was formed during 1 h sintering at 1200°C according to below Equation:

$$CaO + MgSiO_3 + SiO_2 \rightarrow CaMgSi_2O_6$$
$$\Delta G_{1200\,°C} = -195.12 \text{ KJ·mol}^{-1}·\text{K}^{-1} \tag{7}$$
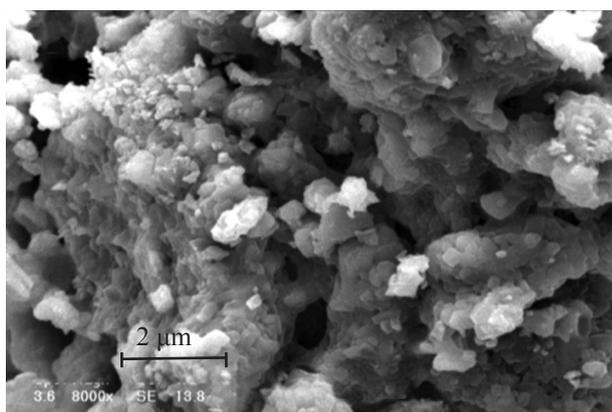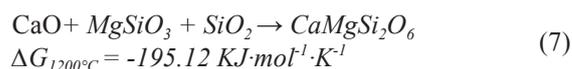
a)
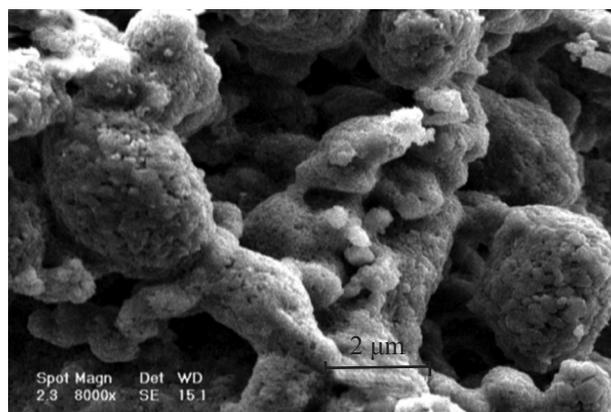
b)
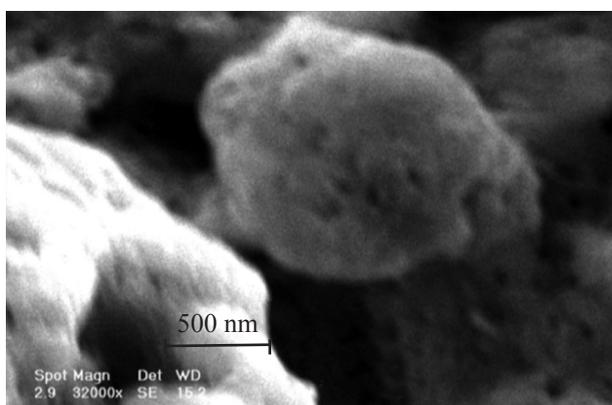
c)
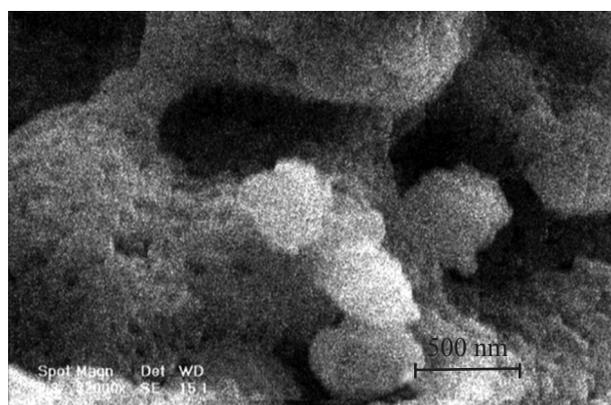
d)

Figure 4. SEM micrographs of prepared powders after 2 h (a, c) and 10 h (b, d) mechanical alloying and subsequent sintering for 1 h.

The adiabatic temperature of Equation 7 was calculated about 502°C. Therefore this reaction was also processed in diffusion mode.

Microstructure evaluation

Figure 4 shows the SEM micrographs of nanocomposite powders after 2 h (a, c) and 10 h (b, d) MA and subsequent sintering at 1200°C for 1 h with different magnifications. As shown the nanocomposite powder for 2 h MA includes very fine agglomerated particles with layer and sphere shapes. By increasing the MA time up to 10 h the agglomerated particles were decreased and their shape were spherical; the agglomerated particles size of nanocomposite powders prepared by 2 h and 10 h MA and subsequent sintering at 1200°C were measured about 1 - 4 μm and 0.4 - 3 μm, respectively.

CONCLUSION

This study is the first report of successfully synthesized the pure forstrite-diopside nanocomposite powder by mechanical alloying and subsequent sintering. Absence of enstatite that causes a reduction in mechanical and bioactivity properties, is an important feature of the prepared powder. The crystallite size of prepared nanocomposite powder was 73 ± 4 nm at 10 h MA and subsequent sintering at 1200°C for 1 h. The agglomerated particles size was in the range of 0.4 - 3 μm. In present study novel mechanism with a new reaction for formation of diopside was reported. MA was used as a novel, simple and economical method for fabrication of this nanocomposite powder.

Acknowledgment

REFERENCES

1. SweenHin T.: *Engineering materials for biomedical applications*, World Scientific Publishing Co. Pte. Ltd, Singapore 596224, 2004.
2. Diba M., Goudouri O.M., Tapia F., Boccaccini A.R.: Current opinion in solid state and materials science *18*, 147 (2014).
3. Ghomi H., Jaberzadeh M., Fathi M.H.: Journal of alloys and compounds *509*, 63 (2011).
4. Ramesh S., Yaghoubi A., Sara Lee k.Y., Christopher Chin K.M., Purbolak sono J., Hamdi M., et al.: Journal of the Mechanical Behavior of Biomedical Materials *25*, 63 (2013).
5. Kharaziha M., Fathi M.H.: Journal of the Mechanical Behavior of Biomedical Materials *3*, 530 (2010).
6. Fathi M.H., Kharaziha M.: Materials Letters *63*, 1455 (2009).
7. Ni S., Chang J., Chou L.: Journal of material Science material in medicine *19*, 359 (2008).
8. Tavangarian F., Emadi R.: Ceramics International *37*, 2275 (2011).
9. Tavangarian F., Emadi R.: Materials Letters *65*, 740 (2011).
10. Teimouri A., Ghorbanian L., Najafi Chermahini A.R., Emadi R.: Ceramics International *40*, 6405 (2014).
11. Nonami T., Tsutsumi S.: Journal of material Science material in medicine *10*, 475 (1999).
12. Razavi M., Fathi M.H., Savabi O., Vashaee D., Taybi L.: Materials science and engineering C *41*, 168 (2014).
13. Iwata N.Y., Lee G.H., Tokuoka Y., Kawashima N.: colloids and surfaces B: Biointerfaces *34*, 239 (2004).
14. Wu C., Chang J.: Journal of Biomedical materials Research part B: Applied biomaterials. *83B*, 153 (2007).
15. Tavoosi M., Enayati M.H., Karimzadeh F.: Journal of alloys and compounds *464*, 107 (2008).
16. Murugan R., Ramakrishna S.: Composite Science and Technology *65*, 2385 (2005).
17. Ali M., Basu P.: Journal of alloys and compounds *500*, 220 (2010).
18. Kheradmandfard M., Fathi M. H.: Ceramics International *39*, 1651 (2013).
19. Hafezi- Ardakani M., Moztarzade F., Rabiee M., Talebi A.R.: Ceramics International *37*, 175 (2011).
20. Williamson G.H., Hall W.H.: Acta Metallurgica *1*, 22 (1953).
21. Tavangarian F., Emadi R.: International Journal of Modern Physics B *24*, 343 (2010).
22. Ptáček P., Lany K., Šoukal F., Opravil T., Bartoníćková E., Tvrdík L.: Journal of the European ceramics society *34*, 515 (2014).
23. MgCO$_3$ (XRD JCPDS data file 01-071-1534)
24. CaCO$_3$ (XRD JCPDS data file 00-005-0586)
25. Talc (XRD JCPDS data file 00-002-0066)
26. CaO (XRD JCPDS data file 00-017-0912)
27. SiO$_2$ (XRD JCPDS data file 00-046-1045)
28. MgO (XRD JCPDS data file 01-071-1176)
29. Lee S.K.Y., Tan C.Y., Lai S.K.L., Tolouei R., Amiriyan M., Yap B.K., et al.: conference (NPC) 1, 19 (2011).
30. MgSiO$_3$ (XRD JCPDS data file 00-022-0714)
31. Mg$_2$SiO$_3$ (XRD JCPDS data file 00-004-0768)
32. CaMgSi$_2$O$_6$ (XRD JCPDS data file 01-072-1497)
33. Ni S., Chou L., Chang J.: Ceramics International *33*, 83 (2007).
34. Mielcarek W., Nowak- Woźny D., Prociów K.: Journal of the European ceramics society *24*, 3817 (2004).
35. Munir Z.A.: American Ceramic Society Bulletin *67*, 342 (1988).
36. Brindley G.W., Hayami R.: Philosophical Magazine Letters *12*, 505 (1965).